Journal of *Marine Science and Engineering*

MDPI

Article

Numerical Study on the Interaction between Ocean Current Power Generator and Unmanned Underwater Vehicle

Shenggui Wang [1,2], Jiyuan Sun [3], Bowen Zhao [3], Yingying Yun [3] and Bin Huang [3,4,*]

[1] School of Materials Science and Engineering, Central South University, Changsha 410083, China
[2] Kunming Branch of the 705 Research Institute, China State Shipbuilding Corporation Limited, Kunming 650032, China
[3] Ocean College, Zhejiang University, Zhoushan 316021, China
[4] The Engineering Research Center of Oceanic Sensing Technology and Equipment, Ministry of Education, Zhejiang University, Zhoushan 316021, China
* Correspondence: binhuang@zju.edu.cn; Tel.: +86-183-6800-8216

Abstract: The unmanned underwater vehicle (UUV) can effectively utilize marine renewable energy after equipping the UUV with an accompanying power generator that improve its long-range endurance. In order to study the interaction between the UUV and the ocean current power generator, a coupled hydrodynamic model of the counter-rotating type turbine and the UUV hull was established. Based on the RANS model and the sliding grid method, this paper analyzed the influence of the ocean current power generator on the straight-ahead resistance and hydrodynamic coefficient of the UUV in the non-working state, and calculated the UUV yaw moment and its surrounding flow field characteristics with the power generator in the working state. Then, the effect of the drift angle on the performance of the counter-rotating type turbine was explored. The results show that the straight-ahead resistance of the UUV increased slightly after equipping the power generator, but the increase was within 14%, and the characteristics of the surrounding flow field of the UUV did not changed greatly. The difference in the linear hydrodynamic coefficients before and after equipping the UUV with the power generator was within 7%. At most drift angles, when the generator was in the working state, the yaw moment of the hull was greater than the condition when the generator was not equipped. Nevertheless, the overall trend of the two sides was similar, so the rotation of the counter-rotating type turbine did not reduce the stability of the hull in the moored state. In addition, when the drift angle was greater than 50°, the UUV hull had a great impact on the performance of the counter-rotating type turbine; the power coefficient C_P and thrust coefficient C_T increased by about 35.7% and 17.8%, respectively. This paper provides a good reference value for the design of the power generation mode of the UUV equipped with a counter-rotating type turbine.

Keywords: current energy; counter-rotating type turbine; ocean energy; RANS; sliding grid

Citation: Wang, S.; Sun, J.; Zhao, B.; Yun, Y.; Huang, B. Numerical Study on the Interaction between Ocean Current Power Generator and Unmanned Underwater Vehicle. *J. Mar. Sci. Eng.* **2022**, *10*, 1869. https://doi.org/10.3390/jmse10121869

Academic Editor: Timothy F. Miller

Received: 30 October 2022
Accepted: 28 November 2022
Published: 2 December 2022

1. Introduction

Since the 21st century, the unmanned underwater vehicle (UUV) has gradually become an important strategic research target. The UUV can perform marine resource exploration, marine environment observation, and underwater military reconnaissance missions, with autonomous navigation capabilities. The main challenges it currently faces are the limitations of underwater positioning and communication systems, as well as limited endurance [1–5]. Regarding the battery life of the UUV, most unmanned underwater vehicles currently provide power sources through lithium batteries or fuel cells. Salazar et al. [6]. found that when the battery was operated under low temperature conditions, the life of the battery was shortened due to the increase in internal resistance, resulting in a decrease in capacity. A thermal management system was developed to control the temperature of the battery. Toh et al. [7] studied a lithium iron phosphate (LiFePO4) battery-powered system

for deep-water emergency operations with autonomous and intelligent battery management technology, which can better utilize the battery's potential capacity and maximize the battery's cycle life. Alejandro Mendez et al. [8] found that the use of a hybrid fuel cell secondary battery power system could reduce the size of components and improve the overall efficiency. The power battery is the main energy supply method for UUV at present, but a single charge cannot make the UUV complete all navigation tasks, and the second charge must return to the flight or reach a fixed charging point, which has become the main difficulty restricting the development of UUVs [9–11]. Therefore, solving the problem of the UUV's battery life and realizing its long-duration and long-range work requirements have gradually become the focus of UUV research.

At present, some researchers tried to use new ways to supply power to the UUV [12,13]. Javier Sosa et al. [14] proposed a new charging method for an underwater battery-free sensor node network to improve the charging efficiency. Hyeung-Sik Choi et al. [15] studied a new integrated platform of unmanned surface vehicles (USVs) and unmanned underwater vehicles (UUVs) connected by underwater cables, which supplied power from USV to UUV to realize real-time motion coordination control between them. In recent years, most of the world's countries and organizations have formulated plans and issued a series of relevant support policies for marine renewable energy (MRE), including offshore wind power, tidal currents, ocean currents, wave energy, etc. [16–19] Zhang et al. [20] has designed a multidirectional energy harvesting device for the UUV that can capture energy from multiple directions and different currents, such as waves and tidal currents, by using oscillating ellipsoid hydrofoils and swing arms. Ding et al. [21] proposed an energy generator based on ocean kinetic energy to meet the energy requirements of UUV detection modules for long-term continuous operation in shallow water, which can meet the energy requirements in general sea conditions. The technology of realizing self-powered underwater vehicles based on ocean thermal gradients and salinity gradients is also a hot research topic, but the technology is not yet mature [22]. In addition, there are huge reserves of ocean current energy resources and a wide distribution range in deep-sea waters. According to the current technology, the power capacity for developing the global ocean current energy is about 75 million kW, and that in Europe is 11 million kW. The UK and France have the highest ocean current power generation (approximately 6 million kW and 3.4 million kW, respectively) [23]. Since the working environment of the UUV is a deep water area, ocean current energy resources are abundant, and their availability and power density are higher than wave energy, temperature difference energy, and other resources [24–27]. Therefore, it is of great strategic significance to study the application of ocean current energy power generators in UUVs.

There are many structures of ocean current power generators, but turbines with a horizontal axis and vertical axis are the mainstream forms. Moreover, the research and application are mostly concentrated on large-scale units with commercial prospects, which are rarely used in unmanned underwater vehicles or deep seawater observation platforms [28–30]. The installation of ocean current power generators on the UUV can better avoid problems, such as poor endurance and low charging efficiency, and the self-power generator can efficiently utilize renewable energy, such as wave energy or ocean current energy, which greatly improves the endurance of the UUV. The vehicle is equipped with an ocean current power generator to generate power by itself, and directly supplies power to the battery to achieve self-sufficiency in electric energy. Tian et al. [31] designed a vertical-axis ocean current power generator for underwater vehicles in view of the energy supply during the navigation of underwater vehicles, and provided prediction and guidance for the actual design and installation work through numerical simulation. Van Thanh Tien Nguyen et al. [32,33] proposed an artificial intelligence algorithm to improve the performance of the centrifugal pump in terms of pump head, pump efficiency, and power, and they optimized the structure of the shell. The efficiency of the pump was increased by about 70%. This method provides a new research idea for improving the ocean current power generation device. Zhao et al. [34] designed a low-power energy

collection system of ocean current energy power generation, which realized the functions of energy capture and electric energy storage. In addition, in the performance study of the counter-rotating type turbine, Samura et al. [35] provided a contra-rotating tidal current power device composed of a special generator with tandem propellers and double rotating armatures for the offshore verification test, which could obtain higher output power under the specified tip speed ratio. Huang and Kanemoto et al. [36] conducted an experimental test of the counter-rotating propellers of tidal turbines in a water tunnel, and found that the predicted value of CFD (Computational Fluid Dynamics) was in good agreement with the experimental value. Jung et al. [37] improved the performance of the counter-rotating propellers based on the numerical algorithm of response surface analysis and adaptive single-objective optimization. Lee et al. [38] conducted an experimental and numerical research on the performance of the counter-rotating propellers under oblique flow conditions, and found that when the angle between the incoming flow and the propeller was 30 degrees, the performance decreased by about 20%. Huang et al. [39] found that the power coefficient of the counter-rotating type turbine was improved compared with the single-propeller turbine; moreover, the wake flow and additional torque were eliminated due to the reverse rotation of the front and rear propellers, thus ensuring that the impact was minimized in the different power generation state after equipping the UUV with an ocean current energy power generator.

In summary, the UUV equipped with an ocean current energy power generator can make full use of marine renewable energy, but after equipping with the power generator, the hydrodynamic coefficient of the UUV and the surrounding flow field may have some changes, particularly as to whether the drift angle affects the counter-rotating type turbine. At present, there are few reports on these aspects. This paper calculates the motion stability of a UUV equipped with the counter-rotating current power generator based on the CFD technology, then studies the interaction between the counter-rotating current power generator and the UUV.

2. Methodology

2.1. Governing Equations

The three conservation equations of fluid flow are the mass conservation equation, the momentum conservation equation, and the energy conservation equation. Fluid is compressible, but in the hydrodynamic research of ships or submersibles, the water can be regarded as an incompressible fluid, which is true in general, and the velocity field and pressure field can be derived by the following formulas:

$$\frac{\partial u_i}{\partial x_i} = 0 \tag{1}$$

$$\frac{\partial u_i}{\partial t} + \frac{\partial (u_i u_j)}{\partial x_j} = -\frac{1}{\rho}\frac{\partial p}{\partial x_i} + \frac{\partial}{\partial x_j}\left[\mu\left(\frac{\partial u_i}{\partial x_j} + \frac{\partial u_j}{\partial x_i}\right)\right] \tag{2}$$

In order to accurately simulate the turbulent motion, the variables in the equation need to be decomposed into two parts: time-averaged and pulsating:

$$\phi = \overline{\phi} + \phi' \tag{3}$$

Then the time average of both sides of the equation can be obtained to calculate the RANS (Reynolds Averaged Navier–Stokes) equation for incompressible fluids:

$$\frac{\partial u_i}{\partial x_i} = 0 \tag{4}$$

$$\frac{\partial (\rho u_i)}{\partial t} + \frac{\partial \left(\rho u_i u_j\right)}{\partial x_j} = f_i - \frac{\partial p}{\partial x_i} + \frac{\partial}{\partial x_j}\left[\mu\left(\frac{\partial u_i}{\partial x_j} + \frac{\partial u_j}{\partial x_i}\right)\right] - \frac{\partial \left(\rho \overline{u_i' u_j'}\right)}{\partial x_i} \tag{5}$$

where u_i is the time-averaged velocity component $(u_1 = u, u_2 = v, u_3 = w)$ in the direction of the Cartesian coordinate system $x_i (i = 1, 2, 3)$, ρ is the mass density of fluid water, t is the time, p is the time-averaged pressure, μ is the molecular viscosity coefficient, f_i is the component of the external force in the x_i direction, u_i' is the pulsating velocity component in the Cartesian coordinate $x_i (i = 1, 2, 3)$ direction, and $\rho\overline{u_i'u_j'}$ is the Reynolds stress tensor [40].

2.2. Performance Coefficients of the Counter-Rotating Type Turbine

The hydrodynamic performance coefficients of the current energy turbine include the power coefficient C_P and thrust coefficient C_T. The power coefficient C_P represents the efficiency of the blades in converting the kinetic energy of the water flow into mechanical energy. The larger the value, the higher the power output of the turbine. The thrust coefficient C_T is a dimensionless parameter representing the axial thrust of the blade, and the calculation formula is as follows [41]:

$$\lambda_i = \frac{\omega_i R_i}{V_{in}} (i = F, R) \tag{6}$$

$$\lambda_T = \lambda_F + \lambda_R \tag{7}$$

$$C_{Pi} = \frac{M_i \omega_i}{(1/2)\rho V_{in}^3 A_i} (i = F, R) \tag{8}$$

$$C_{PT} = C_{PF} + C_{PR} \tag{9}$$

$$C_{Ti} = \frac{T_i}{(1/2)\rho V_{in}^2 A_i} (i = F, R) \tag{10}$$

$$C_{TT} = C_{TF} + C_{TR} \tag{11}$$

where λ is the tip speed ratio (TSR), ω is the blade rotation angular velocity (unit: rad/s), R is the blade radius (unit: m), V is the inflow velocity of the hydraulic turbine (unit: m/s), A is the swept area of the blade, M is the torque of the hydraulic turbine (unit: N · m), T is the axial thrust received by the hydraulic turbine (unit: N), and subscripts F and R represent the front and rear propellers, respectively.

3. Computational Model and Meshing

3.1. Geometric Model

The UUV design in this paper is based on the fully attached SUBOFF model, which was proposed by the U.S. Defense Advanced Research Projects Agency (DARPA), and includes an axisymmetric body, podium enclosure, a tail rudder, and other attachment combinations. The main body of the ocean current power generator is a counter-rotating type turbine. The geometric model and related parameters are shown in Figures 1 and 2 and Table 1, respectively. The current energy generator is installed at the center of gravity of the hull.

(**a**) (**b**)

Figure 1. Geometric model: (**a**) UUV model; (**b**) Ocean current power generator.

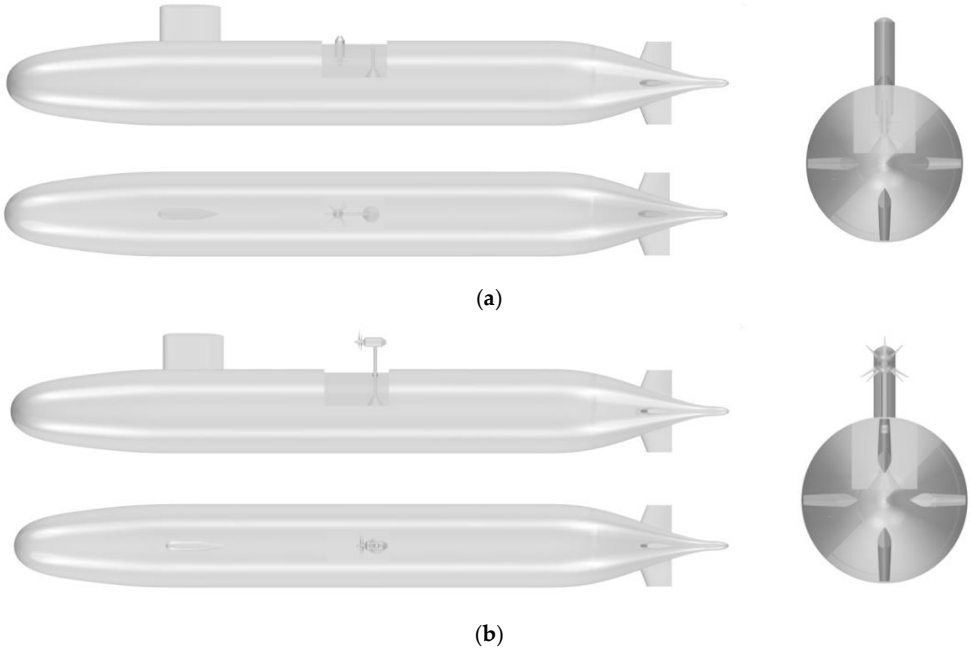

(**a**)

(**b**)

Figure 2. Three views of model: (**a**) Non-working state; (**b**) Working state.

Table 1. Model parameters.

	Main Features	Parameter Value
UUV	Length (L_{OA})	26.136 m
	Length between perpendiculars (L_{BP})	25.566 m
	Maximum hull diameter (D)	3.048 m
Ocean current energy generator	Diameter of front propeller (D_f)	1000 mm
	Diameter of rear propeller (D_f)	950 mm
	diameter ratio	0.95
	Axial distance between front and rear propellers	90 mm

3.2. Calculation Conditions

In this paper, the $SST\ k-\Omega$ model is selected, and the UUV is placed in an infinitely deep seawater area. The $SST\ k-\Omega$ model includes the transmission of turbulent shear stress, which can accurately predict the beginning of flow and the separation amount of fluid under a negative pressure gradient. For the calculation domain selection, this paper selects a three-dimensional cuboid-shaped watershed whose axis coincides with the symmetry axis of the UUV model. Taking the center of gravity of the UUV as the coordinate origin, extend $2.5L_{OA}$ forward to the front face, and extend $3L_{OA}$ backward to the rear face, with a distance of $8D$ from the surrounding sides. The front and side surfaces are set as the velocity inlet, the inflow velocity is given, the rear face is set as the pressure outlet, the reference pressure is a standard atmospheric pressure, and the relative pressure is zero. The surface of the hull is set as a non-slip wall. The final computational domain and boundary conditions are shown in Figure 3. In the process of numerical simulation of the counter-rotating type current energy generator in the non-working state, the drift angle and attack angle are respectively changed in the horizontal and vertical planes of the hull to calculate the oblique sailing. The range of the drift angles and attack angles is -6° to 6°, and the velocity of the UUV in the oblique sailing state is 7.46 m/s.

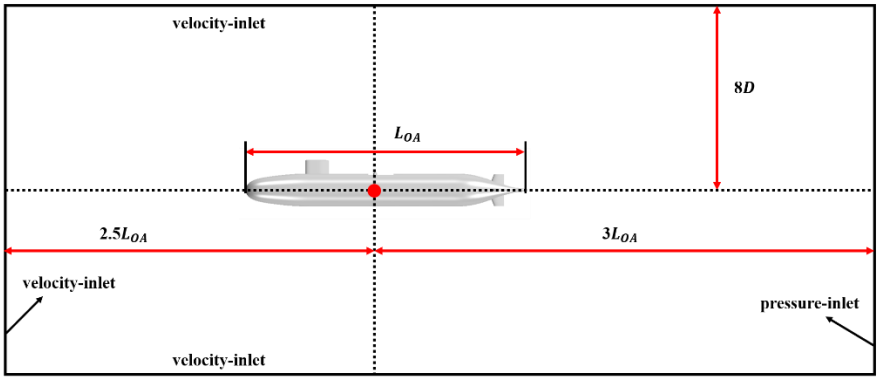

Figure 3. Computational domain and boundary conditions.

The model includes numerical simulation of the counter-rotating type current energy generator in the working state. The turbine is lifted by the landing gear, and the main part of the generator is exposed outside the UUV cabin. Both front and rear propellers rotate at an angular velocity of 12 rad/s in opposite directions to help to eliminate wake flow and additional torque. When the power generator is working, the UUV hull is in a moored state. At this time, the influence of the large drift angle on the hull force and the performance of the counter-rotating type turbine is mainly studied. The drift angles range from 0° to 90°, a set of data is calculated per 10°, and the current velocity is 1.5 m/s.

3.3. Determining Grid Size Based on GCI

The impact of grid on the CFD numerical simulation is particularly important. In most cases, the more dense the grid is, the smaller the GCI (Grid Convergence Index) index, and the more accurate the calculation results [42,43]. The GCI method requires at least three types of meshes from coarse to fine. The mesh size selected for the calculation of mesh convergence in this experiment is: grid h_1: 0.113 m, grid h_2: 0.160 m, grid h_3: 0.226 m, so the grid encryption factor r is:

$$r_{21} = \frac{h_2}{h_1} = \sqrt{2} = r_{32} = \frac{h_3}{h_2} \tag{12}$$

At this time, the r value is greater than the recommended minimum grid encryption factor 1.3, and the calculation steps of the GCI are [44]:

(1) Calculation convergence accuracy p:

$$p = \frac{1}{ln(r_{21})}\left|ln\left|\frac{\varepsilon_{32}}{\varepsilon_{21}} + q(p)\right|\right| \tag{13}$$

$$q(p) = ln\left(\frac{r_{21}^{p} - s}{r_{32}^{p} - s}\right) \tag{14}$$

$$s = 1 \cdot sign\left(\frac{\varepsilon_{32}}{\varepsilon_{21}}\right) \tag{15}$$

$$\varepsilon_{21} = \phi_2 - \phi_1 \tag{16}$$

$$\varepsilon_{32} = \phi_3 - \phi_2 \tag{17}$$

where ϕ_i is the discrete value of simulation calculation under the i grid, and when $x > 0$, $sign(x) = 1$, $x = 0$, $sign(x) = 0$, or $x < 0$, $sign(x) = -1$. In this numerical simulation, $r_{21} = r_{32} = \sqrt{2}$, which can calculate $q(p) = 0$, and then simplify the calculation of convergence accuracy p.

(2) When calculating grid 2 compared to the relative error of grid 1, based on Formula (18), it can also calculate the relative error of grid 3 relative to grid 2:

$$e_a^{21} = \left| \frac{\phi_2 - \phi_1}{\phi_1} \right| \tag{18}$$

(3) When calculating grid 2 compared with the grid convergence index of grid 1, based on Formula (19), it can also calculate the grid convergence index of grid 3 relative to grid 2:

$$GCI_{21} = \frac{1.25 e_a^{21}}{r_{21}^p - 1} \tag{19}$$

Based on the commercial CFD software, the straight-ahead resistance value of the UUV is calculated under the three grids of coarse, medium, and fine. The velocity is 3.048 m/s. The calculation results are shown in Figure 4. The calculation results of the three grids were close. Their relative errors were smaller than 2%, and the calculation resistance value of grid 1 was greater than the calculation results of grid 2 and grid 3. GCI method was used to evaluate the numerical error, $GCI_{21} = 0.45\%$, $GCI_{32} = 0.07\%$. It can be seen that the difference between the calculation results of grid 2 and grid 3 was very small. GCI_{21} was also less than 5%, which met the convergence conditions. In order to ensure the calculation accuracy and improve the calculation efficiency, the size of grid 2 (0.160 m) was selected for subsequent calculation. Figure 5 shows the distribution of Y+ values on the UUV surface after using the medium grid. It can be seen that the Y+ values were less than 5, which met the calculation requirements [45].

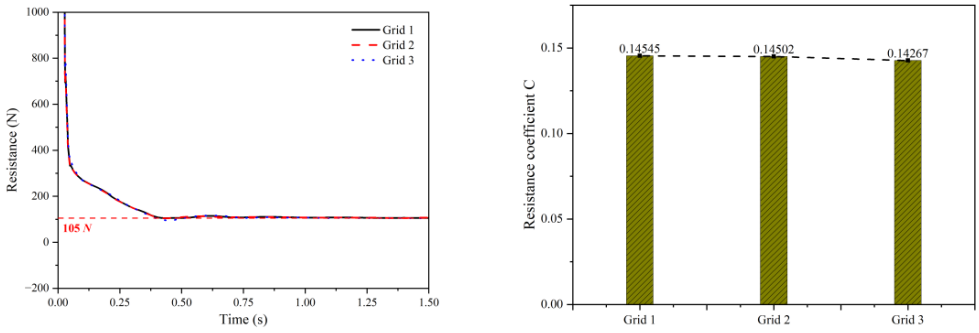

Figure 4. Mesh convergence results: (**a**) Straight-ahead resistance time curve; (**b**) Resistance coefficient of UUV with three grids.

Figure 5. The distribution of Y+ values on the UUV surface after using the medium grid.

The mesh division adopted the hexahedral mesh. In order to better capture the flow details, it was necessary to refine the mesh around the hull and its wake. The mesh is shown in Figure 6, and the UUV surface mesh is shown in Figure 7.

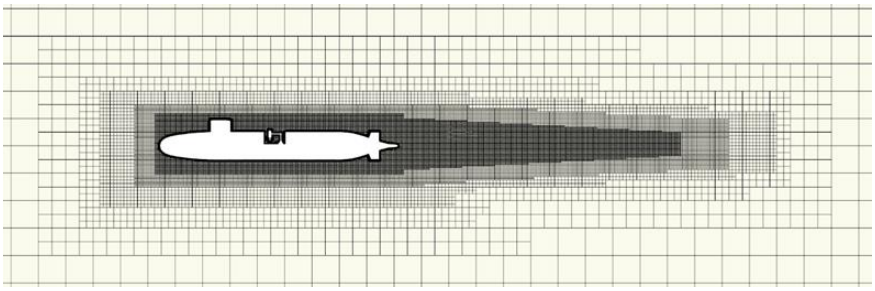

Figure 6. Meshing of the computational domain (non-working state).

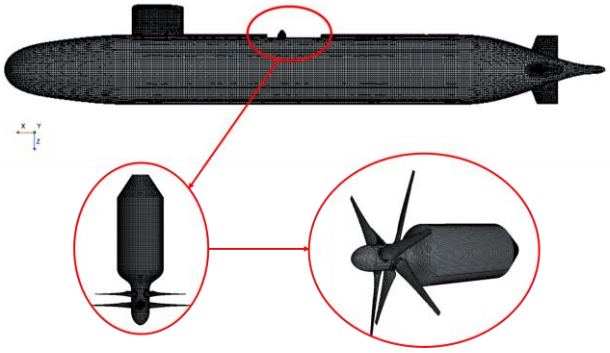

Figure 7. UUV surface mesh.

3.4. Sliding Grid

For the counter-rotating type turbine in the working state, the transient sliding grid needed to be calculated. According to the position of the front and rear propellers of the counter-rotating type turbine, two rotation domains were divided, including the front propeller and the rear propeller, respectively. The meshing method was similar to Huang et al. [46]. From the direction of the flow (the direction of the velocity inlet), the rotation direction of the front blade was counterclockwise, and the rotation direction of the rear blade was clockwise. As the right-hand grip rule, the front and rear propellers' rotation angular velocity were 12 rad/s and −12 rad/s, respectively. When dividing the mesh, the rotation domain and the calculation domain formed two slip interfaces to transmit grid calculation information. The mesh in the rotation domain needed to be refined to ensure the correct solution of the rotating motion of the propellers. As shown in Figure 8, the number of grids in the front propeller area was 244,700, and the number of grids in the rear propeller area was 148,100. Figure 9 shows the grid results of the final calculation domain, and the number was 3,204,900. The solver selected the implicit non-steady state, the time discrete format was first-order, and the time step was 0.00145 s to ensure the accuracy of the calculation results.

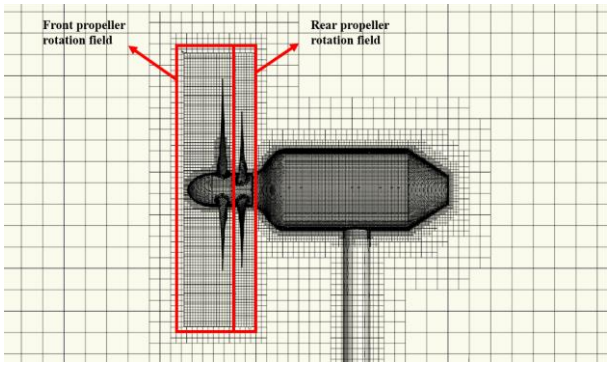

Figure 8. Sliding grid.

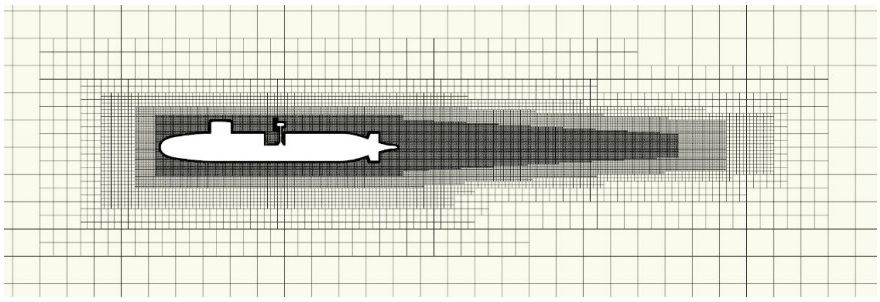

Figure 9. Meshing of the computational domain (working state).

4. Calculation Results and Analysis in Non-Working State

4.1. UUV Resistance in Straight-Ahead

In this section, the resistance values of the UUV at six velocities were calculated first, as shown in Figure 10. By comparing the resistance coefficients of the UUV equipped with the power generator with the fully attached SUBOFF, it was found that the straight-ahead resistance of the UUV in the range of $0.4 < Fr < 1.5$ increased slightly after the power generator was equipped, but the increase amplitude was within 14%, which indicated that the power generator did not have a significant impact on the straight-ahead resistance of the UUV.

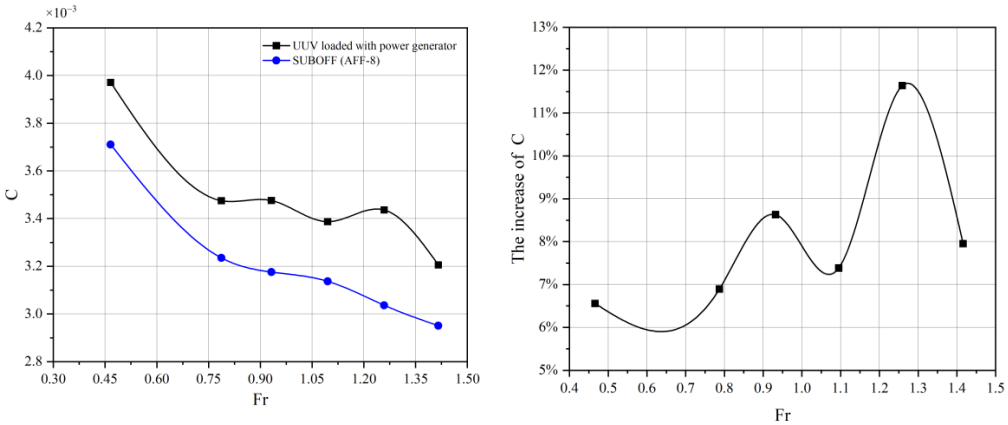

(**a**) (**b**)

Figure 10. Resistance calculation results of UUV at different speeds: (**a**) Resistance coefficient; (**b**) The increase of UUV resistance coefficient at different speeds.

4.2. Characteristics of Flow Field around the UUV

In order to explore the influence and action mechanism on the hydrodynamic performance of the hull after equipping it with the ocean current energy power generator, in this section, we compared the flow field around the UUV with the flow field of the fully attached SUBOFF (mainly the velocity field, pressure field, and vorticity field). The velocity field of the mid-longitudinal plane and the horizontal plane are shown in Figures 11 and 12, respectively. By comparing the velocity field of the mid-longitudinal plane, it could be found that the difference between the two was only at the power generator. The reason is that the motor is in a non-working state at this time, and the motor is exposed outside the cabin, which hinders the movement of the surrounding flow field and increases the resistance to a certain extent. The power generator equipped at the center of gravity is far away from the UUV enclosure, so the enclosure and the power generator do not interfere with each other in the flow field. Comparing the velocity fields on the horizontal plane, it can be seen that the two flow fields were almost identical.

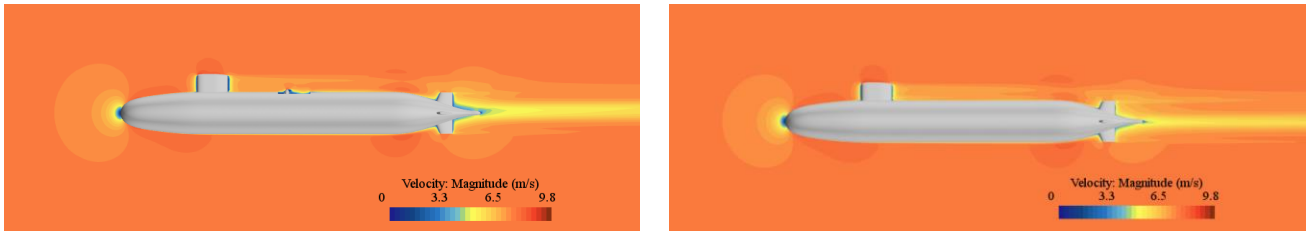

(**a**) (**b**)

Figure 11. Velocity nephograms in mid-longitudinal plane: (**a**) UUV equipped with power generator; (**b**) SUBOFF (AFF-8).

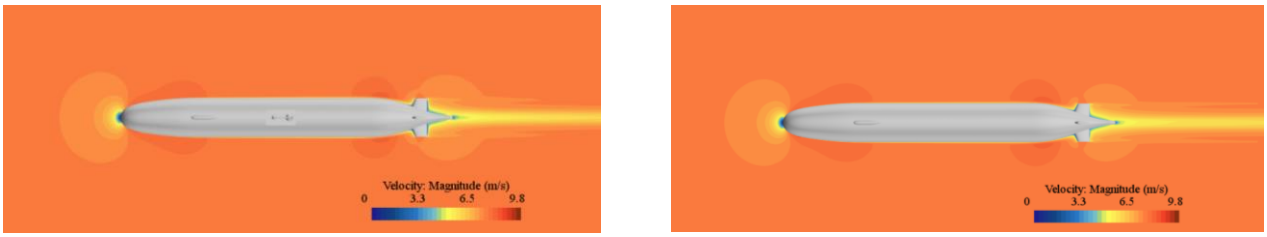

(**a**) (**b**)

Figure 12. Velocity nephograms in horizontal plane: (**a**) UUV equipped with power generator; (**b**) SUBOFF (AFF-8).

Figure 13 shows the velocity distribution of the propeller plane at the rear of the hull at $x/L = 0.978$. It can be seen that a V-shaped flow field area was formed around the upper tail rudder due to the influence of the enclosure on the wake field, and it presented a Clover-shaped flow field area. In addition, due to the influence of the power generator on the wake field, the V-shaped flow field area expanded, and the velocity of the trailing edge of the tail rudder was significantly higher than that of the surrounding area. After the power generator was equipped, the velocity field at the propeller plane did not change much, which means that the propeller's advance speed, thrust, and efficiency were negligibly affected by the power generator.

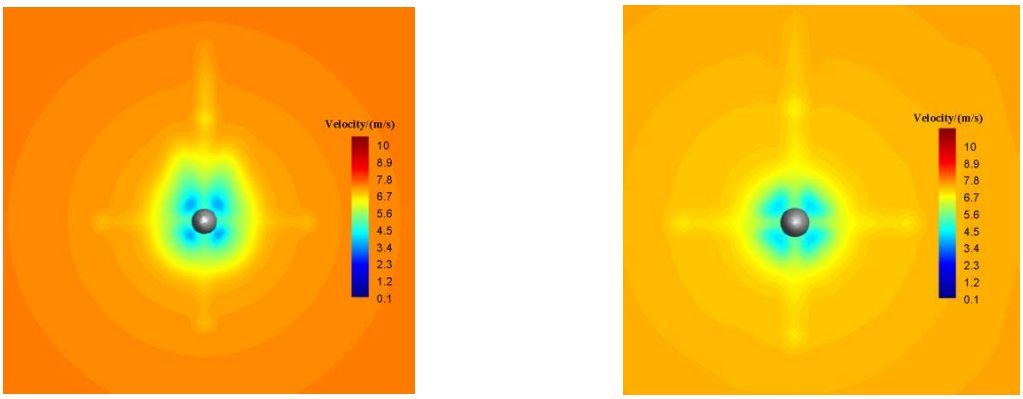

(**a**) (**b**)

Figure 13. Velocity nephograms at the propeller plane($x/L = 0.978$): (**a**) UUV equipped with power generator; (**b**) SUBOFF (AFF-8).

Figures 14 and 15 are the nephograms of the surface pressure distribution of the UUV equipped with the power generator and the fully attached SUBOFF. The pressure at the hull bow, enclosure, and the front end of the stern rudder was relatively large, because the fluid movement in these three areas was blocked and the flow velocity decreased, which is consistent with the actual flow field environment. The pressure field at the current power

generator is shown in Figure 16, and the pressure in the cabin was slightly lower than the surface of the hull. In the upstream direction, the motor and the rear edge of the cabin generated a high pressure area, and the strength requirements of these two places were guaranteed in the design. In general, the characteristics of the flow field around the UUV after equipping it with the power generator did not change greatly.

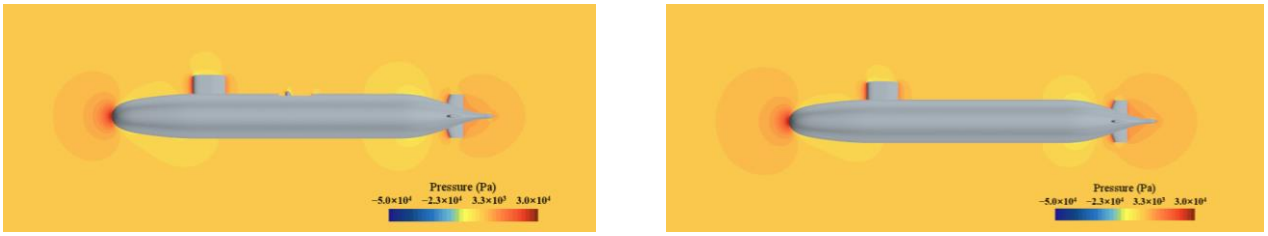

(**a**) (**b**)

Figure 14. Pressure nephograms in mid-longitudinal plane: (**a**) UUV equipped with power generator; (**b**) SUBOFF (AFF-8).

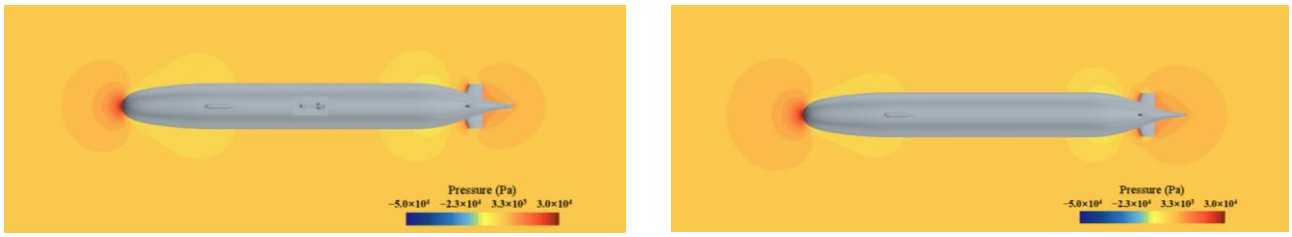

(**a**) (**b**)

Figure 15. Pressure nephograms in horizontal plane: (**a**) UUV equipped with power generator; (**b**) SUBOFF (AFF-8).

(**a**) (**b**)

Figure 16. Pressure distribution at the ocean current power generator: (**a**) Vertical view; (**b**) Front view.

Figure 17 shows the vortex structure of the UUV with the power generator and the fully attached SUBOFF in the oblique sailing state, which was described based on the Q criterion, where the Q value is 5, and the hull drift angle is 4°. The similarities between both models are that there is a thick layer of attached vortices in the inflow and outflow sections of the main hull, and vortex shedding occurred in a staggered distribution at the parallel mid-body. Horseshoe vortices were generated at the contact part of the enclosure and the empennage with the main hull. The wake vortex at the top and trailing edge of the enclosure also had a necklace shape. In contrast to the necklace vortex pair of the hull, the necklace vortex at the top of the enclosure was thicker, and was more obviously affected by the drift angle changing and flow separation. The difference is due to the fact that the exposed area of the power generator generates a more complex and concentrated vortex

structure, because the fluid velocity at different vertical positions is quite different, and the mutual disturbance between the fluids is relatively severe.

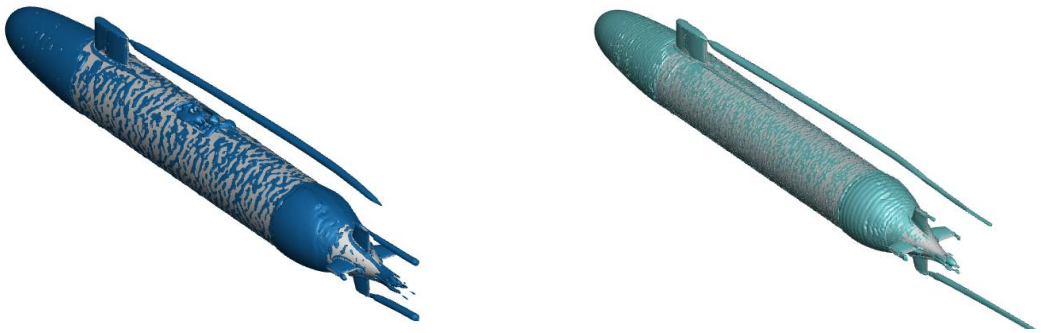

(**a**) (**b**)

Figure 17. Vortex structure comparison: (**a**) UUV equipped with power generator; (**b**) SUBOFF (AFF-8).

The vortex structure at different drift angles in the horizontal plane is shown in Figure 18. At small drift angles of 0° and 2°, there was almost no attached vortex in the parallel middle section of the main hull, and there was no necklace vortex structure at the top and trailing edge of the enclosure. This shows that the change in the UUV-attached vortex system was relatively gentle within the range of small drift angles, and it did not form large-scale vortex system separation, which greatly changes the flow field near the hull and tail rudder. With the increase in drift angle, the attachment vortices of the parallel middle section of the main hull gradually increased, and the necklace vortex of the enclosure gradually stretched into a thin strip along the length direction. The development and detachment speed of the vortex system on the UUV back flow surface were significantly accelerated. The horseshoe vortex and combined vortex in the contact part between the enclosure and the main hull were more obvious, and the vortex system in the stern was more complex, which indicates that the increase in drift angle had adverse effects on the UUV vortex structure. In the range of small drift angles, the change in the UUV attachment vortex system was relatively gentle. With the increase in drift angle, the attachment vortex in the parallel middle section of the main hull gradually increased, and the development and detachment speed of the UUV back flow surface vortex system were significantly accelerated. Therefore, the increase in drift angle had adverse effects on the UUV vortex structure.

4.3. UUV Hydrodynamic Coefficient

The velocity of the UUV in the oblique sailing state was 7.46 m/s. With this velocity, the UUV with the power generator was numerically simulated at different drift angles and attack angles. The drift angle and attack angle varied from $-6°$ to $6°$. The lateral force Y, yaw moment N, vertical force Z, and pitch moment M experienced by the hull under different working conditions were calculated, and the hydrodynamic coefficients were derived. The hydrodynamic coefficient refers to the value of the partial derivative of the hydrodynamic component of the UUV motion parameter at the initial equilibrium point. The trend of dimensionless force and moment changing with drift angle is shown in Figures 19 and 20. It can be seen that the curve is approximately symmetrical about the origin, indicating that the direction of drift angle and attack angle influence the direction of forces and moments. The greater the absolute value of drift angle and attack angle, the more significant the force and moment on the hull. The curve of the hydrodynamic coefficients of the UUV equipped with the power generator almost coincided with the curve of the hydrodynamic coefficients of the fully attached SUBOFF, which indicates that even if the power generator was equipped on the hull, the motion law and state of the UUV in the oblique sailing state were not affected.

The formulas for dimensionless forces and moments are as follows:

$$Y' = \frac{Y}{\frac{1}{2}\rho L^2 U^2} \tag{20}$$

$$Z' = \frac{Z}{\frac{1}{2}\rho L^2 U^2} \tag{21}$$

$$N' = \frac{N}{\frac{1}{2}\rho L^3 U^2} \tag{22}$$

$$M' = \frac{M}{\frac{1}{2}\rho L^3 U^2} \tag{23}$$

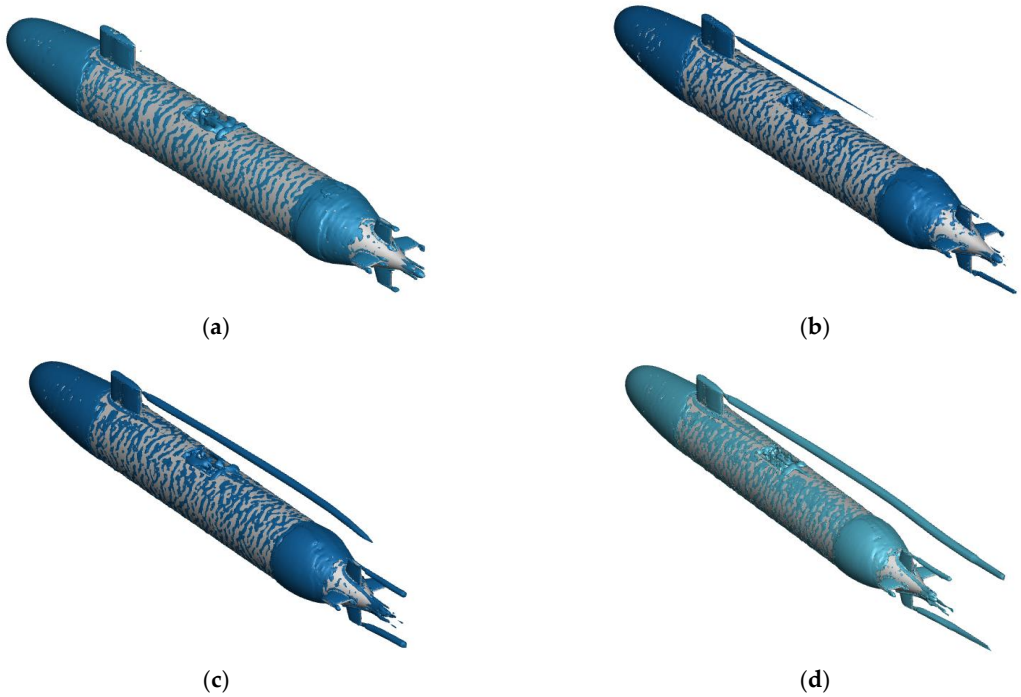

(**a**) (**b**) (**c**) (**d**)

Figure 18. Comparison of vortex structures at different drift angles: (**a**) Drift angle 0°; (**b**) Drift angle 2°; (**c**) Drift angle 4°; (**d**) Drift angle 6°.

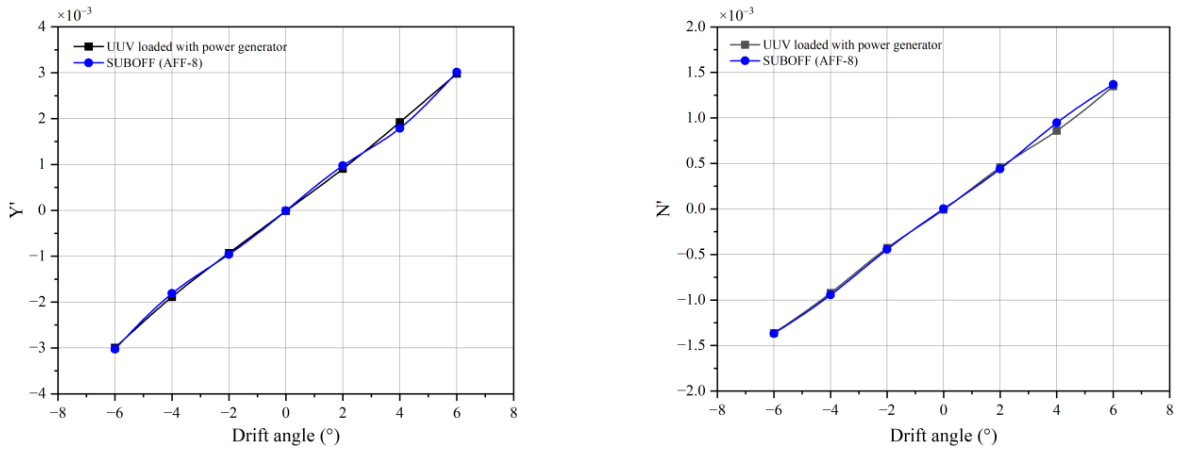

(**a**) (**b**)

Figure 19. Hydrodynamic coefficients of horizontal plane: (**a**) Dimensionless lateral force; (**b**) Dimensionless yaw moment.

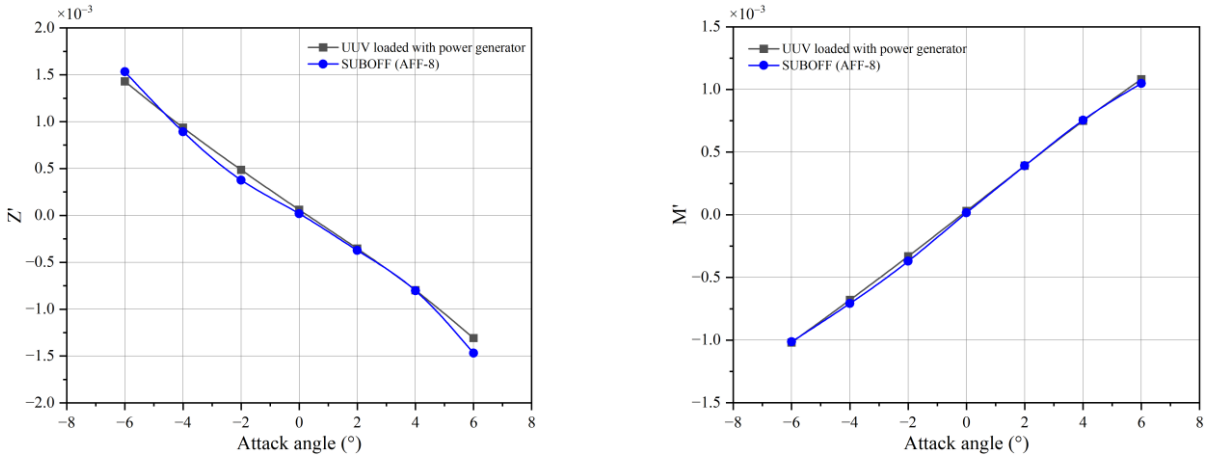

Figure 20. Hydrodynamic coefficients of vertical plane: (**a**) Dimensionless vertical force; (**b**) Dimensionless pitch moment.

The calculation results of the hydrodynamic coefficients are shown in Table 2. The relative error between the first order linear hydrodynamic coefficients of the UUV equipped with power generator and the fully attached SUBOFF was within 7%. In addition, by comparing the forces and moments of the two in Figures 19 and 20, it can be found that whether the power generator was equipped or not had no obvious impact on the force of the hull, and the hydrodynamic characteristics of the hull itself were not affected after the power generator was equipped.

Table 2. Comparison results of hydrodynamic coefficients.

	SUBOFF (AFF-8)			UUV Equipped with Power Generator	
	Experimental Values	Calculated Value	Relative Error	Calculated Value	Relative Error
Y'_v	−0.0278	−0.0279	0.36%	−0.0261	−6.12%
N'_v	−0.0128	−0.0132	3.13%	−0.0133	−3.91%
Z'_w	−0.0139	−0.0135	−2.88%	−0.0129	−7.19%
M'_w	0.0103	0.0102	−0.97%	0.0102	−0.97%

5. Calculation Results and Analysis under Working Conditions

5.1. Yaw Moment of UUV and Its Surrounding Flow Characteristics

When the current power generator is working, the UUV is in moored state. The power generator captures the kinetic energy of the current through the folding mechanism extending out of the cabin, then rotates the counter-rotating propellers, and converts the kinetic energy of the sea water into mechanical energy that further generates electric energy. At this time, the propeller rotation disturbs the flow field around the hull, thus changing the yaw moment of the hull itself and affecting the stability of the UUV during working. In addition, because the direction of the underwater current is uncertain, sometimes the direction of the current is not strictly along the length of the hull, but forms an angle with the hull. The power generator actively rotates through the yaw mechanism to meet the flow of the ocean current so as to ensure the efficiency of power generation to the greatest extent. The rotation of the power generator causes an angle (namely drift angle) between the normal rotation direction of the power generator and the length direction of the hull, which also affects the stability of the UUV when working.

In order to fully explore the influence of the ocean current power generator on the stability of the hull and the flow field around the hull, this paper calculated the yaw

moment coefficient N' of the hull at the drift angles range of 0° to 90° at the incoming flow speed of 1.5 m/s (the current speed when the counter-rotating propellers work), as shown in Figure 21. When the power generator was working, the yaw moment N of the UUV at most drift angles was greater than that when the power generator was not equipped, but the overall trend of the two was similar. When the drift angle was 80°, the yaw moment N of the UUV was 1.58 times than when the power generator was not equipped, and the relative error of the two at other drift angles was within 15%. When the drift angle was greater than 70°, the power generator had a certain impact on the yaw moment of the hull when it was working, but the impact was slight and did not damage the stability of the hull in the moored state within the controllable range.

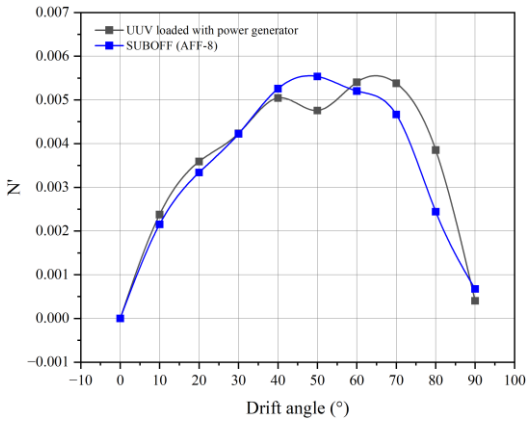

Figure 21. Comparison of yaw moment.

In the process of drift angle change, the yaw moment of the UUV increased first and then decreased. It can be seen from Figure 21 that the critical point was about 50°, that is, when the drift angle of the hull was roughly greater than 50°, the yaw moment N experienced by the hull started to decrease. The yaw moment is closely related to the lateral force on the UUV hull. For this reason, the pressure distribution on the horizontal plane of the hull at different drift angles was analyzed, as shown in Figures 22 and 23. When the drift angle was small, the lateral force on the hull was concentrated at the bow. At this time, the calculation formula of yaw moment $N = FLsin\beta$ (β is drift angle) could be obtained at the moment that N increased with the increase in drift angle. When the drift angle of the hull was greater than about 50°, the lateral force on the rear of the hull gradually increased, thus offsetting the yaw moment generated by a part of the bow. Therefore, the yaw moment N gradually decreased with the increase in drift angle.

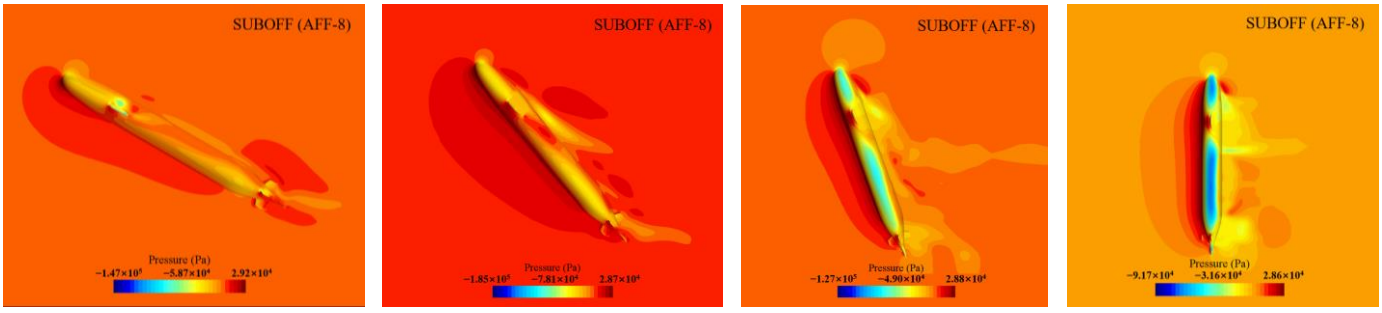

(**a**) (**b**) (**c**) (**d**)

Figure 22. Horizontal pressure distribution of SUBOFF at different drift angles: (**a**) Drift angle 30°; (**b**) Drift angle 50°; (**c**) Drift angle 70°; (**d**) Drift angle 90°.

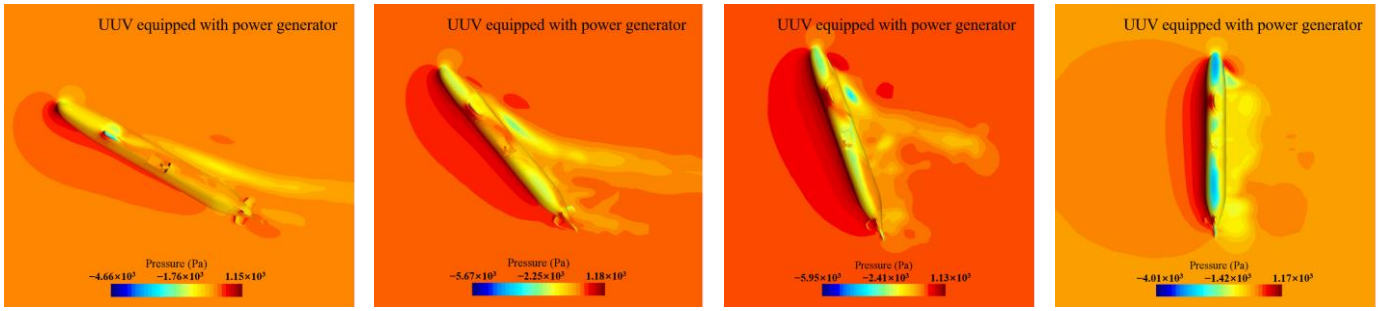

(**a**) (**b**) (**c**) (**d**)

Figure 23. Horizontal pressure distribution of UUV at different drift angles: (**a**) Drift angle 30°; (**b**) Drift angle 50°; (**c**) Drift angle 70°; (**d**) Drift angle 90°.

Figure 24 shows the velocity distribution in the mid-longitudinal plane of the counter-rotating type turbine at different drift angles. When the drift angle was 0°, the flow field of the UUV, except for the area of the current energy generator, was similar to the flow field distribution of the bare hull. Due to the high-speed rotation of the counter-rotating propellers in the working state, and given that the rotation directions of the front and rear propellers were opposite, the velocity of the flow field behind the propellers decreased sharply. As the direction of the ocean current changed, in order to ensure the efficiency of the counter-rotating type current energy generator, the normal direction of the rotation of the blades still needed to maintain the upstream direction, and thus formed a certain angle with the *x*-axis direction of the UUV, which is called the drift angle. As the drift angle increased, a nonlinear vortex street gradually appeared. This phenomenon can be clearly seen from the velocity nephogram with a drift angle of 60°. At this time, the flow field around the UUV and the wake field behind the power generator formed coupling, which caused the wake field of the power generator to show a downward trend.

5.2. Influence of UUV Drift Angle on the Performance of the Hydraulic Turbine

The hydrodynamic characteristics of ocean current turbines include thrust characteristics and power characteristics, which are respectively characterized by the thrust coefficient C_T and power coefficient C_P, both of which are dimensionless. The calculation formulas are shown in Section 2.2. Figure 25 represents the variation trend of the thrust coefficient C_T and power coefficient C_P with the UUV drift angle in the working state of the front and rear propellers of the counter-rotating propellers, respectively. When the drift angle was between 0° and 50°, the C_T and C_P coefficients of the front and rear propellers changed very little, and showed a slight upward trend. The C_T and C_P coefficients of the rear propeller were larger than those of the front propeller, because the number of blades of the rear propeller was four and the number of blades of the front propeller was three, so the thrust generated by the incoming flow of the rear propeller was greater. The vortex energy that was not fully utilized by the front propeller was transferred to the rear propeller, which also increased the axial thrust of the rear propeller, which eventually led to the C_T coefficient of the rear propeller being greater than that of the front propeller. In addition, the diameter of the rear blade was smaller than that of the front blade, and the required torque was smaller at the same rotation speed, so that the C_P coefficient of the rear blade was larger than that of the front blade.

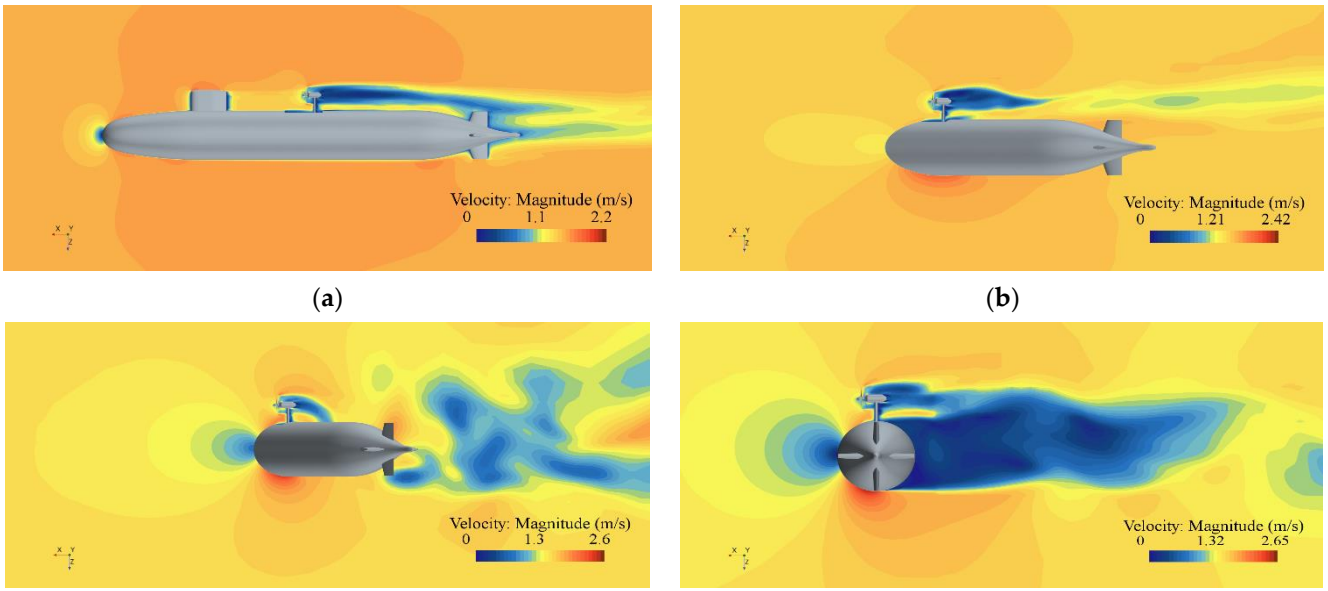

Figure 24. Velocity distribution of the mid-longitudinal section of the counter-rotating type turbine at different drift angles: (**a**) Drift angle 0°; (**b**) Drift angle 30°; (**c**) Drift angle 60°; (**d**) Drift angle 90°.

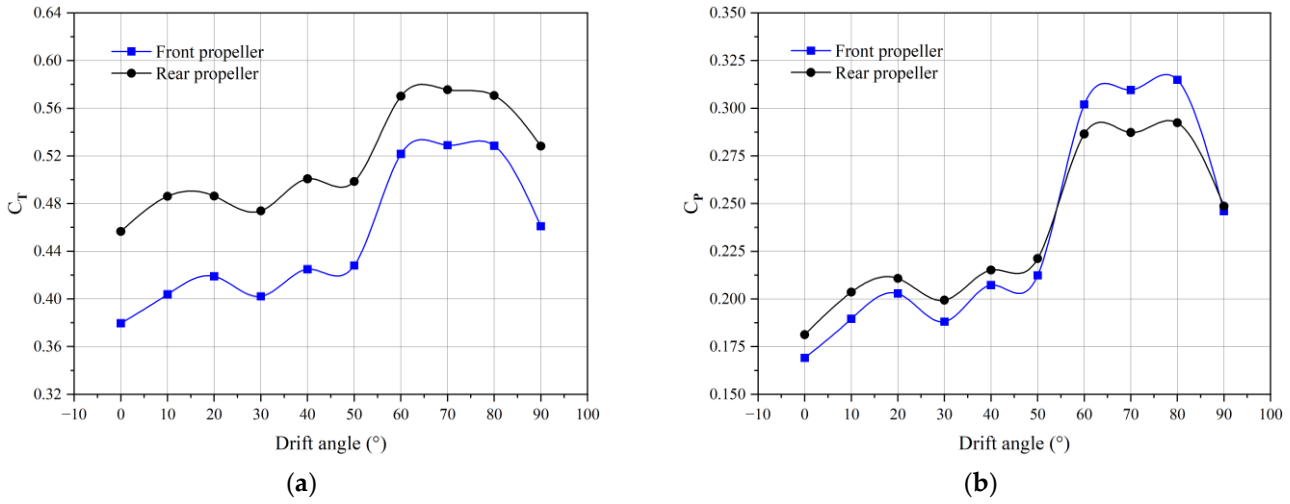

Figure 25. Coefficient of performance of front and rear propellers at different drift angles: (**a**) Thrust coefficient C_T; (**b**) power coefficients C_P.

When the drift angle was between 50° and 60°, the C_T and C_P coefficients had a sudden rise at the same time. Figure 26 shows the velocity distribution of the contra-rotating propellers at the drift angles of 50° and 60°. It can be clearly seen that the velocity distribution of the propellers planes was not uniform at the drift angle 60°. The reason is roughly that the wake of the UUV hull and the wake of the counter-rotating type turbine began to couple with each other at this time, resulting in the expansion of the low-speed area in the velocity field. At the same time, the wake of the turbine was deformed, and the velocity gradient behind the counter-rotating propellers increased, resulting in greater axial thrust and torque.

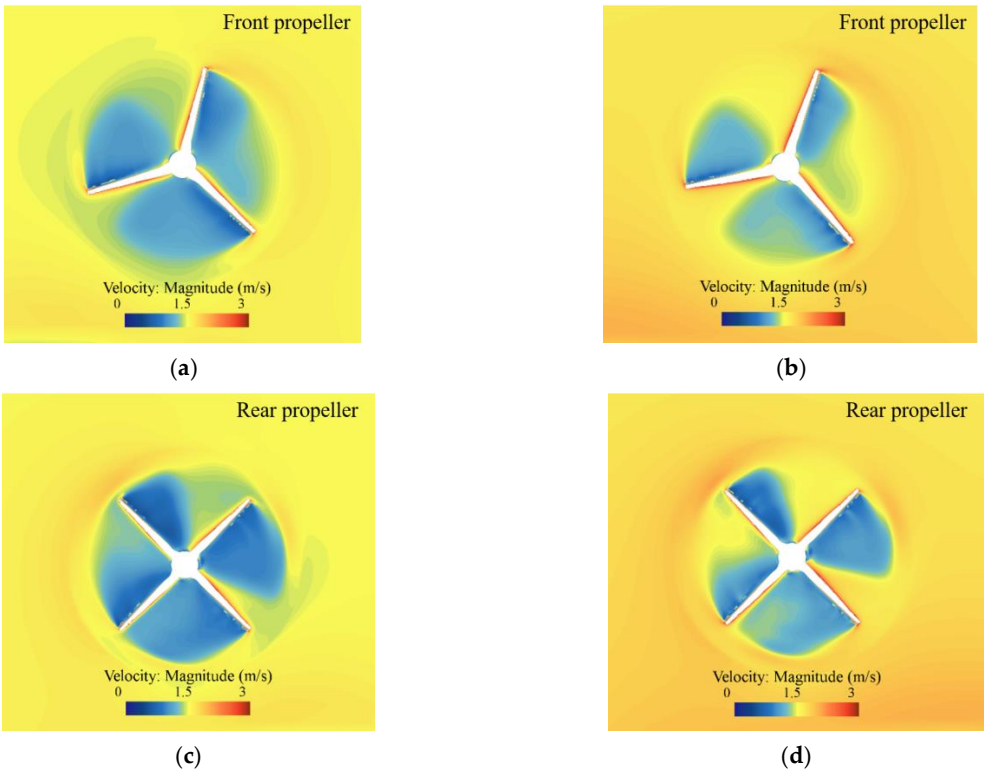

Figure 26. Counter-rotating propellers planes' velocity nephograms at drift angles of 50° and 60°: (**a**,**c**) Drift angle 50°; (**b**,**d**) Drift angle 60°.

When the drift angle was between 60° and 80°, the wake fields of the UUV and turbine were further coupled, and the C_T and C_P coefficients were basically stable at this time. When the drift angle was 80° to 90°, the vortex street phenomenon of the wake on the side of the hull was gradually regular, so that the influence on the wake of the turbine was reduced. When the drift angle was 90°, the wake of the counter-rotating type turbine was the same as the axes of rotation, which were parallel, and the C_T and C_P coefficients were reduced to values for small drift angles. The differences between the C_T and C_P coefficients of the front and rear propellers are shown in Figure 27, and the maximum differences between the two coefficients were 0.0823 and −0.0225, respectively. Finally, the C_T and C_P coefficients of the counter-rotating type turbine at different drift angles are shown in Figure 28.

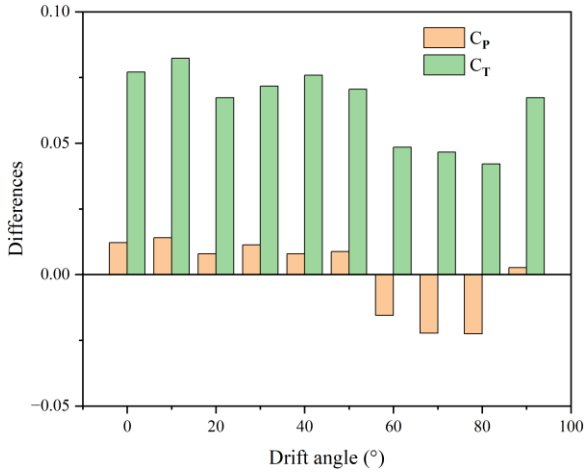

Figure 27. Differences between C_T, C_P of front propeller and rear propeller.

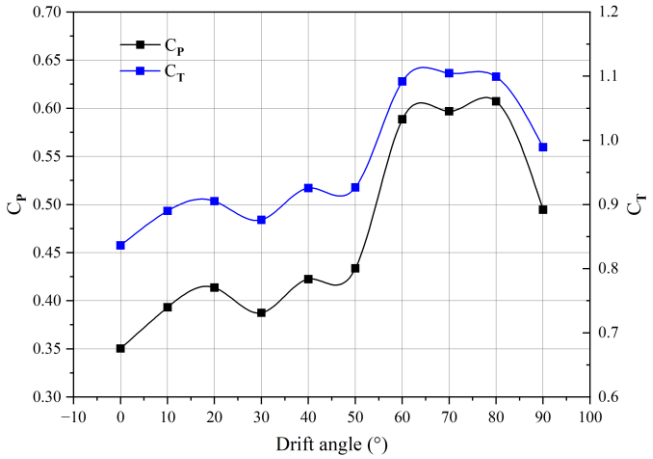

Figure 28. Contra-rotating propeller power coefficient C_P at different drift angles.

6. Conclusions

In this paper, the interaction between the UUV and the ocean current power generator was studied. The key parameters, such as the straight-ahead resistance and the hydrodynamic coefficient of the hull at different speeds, were calculated. Meanwhile, the influence of the yaw moment of the UUV and the hull on the hydrodynamic performance of the counter-rotating type turbine was analyzed. The conclusions obtained in this paper are as follows:

(i) The layout scheme of equipping the UUV with the ocean current power generator to the center of gravity is reasonable. When the power generator was in a non-working state (the generator was retracted into the cabin), although the sailing resistance of the UUV increased slightly, the increase was within 14%, which meant that the power generator did not have a great impact on the straight-ahead resistance of the UUV. The power generator equipped at the center of gravity was far away from the UUV enclosure, so the enclosure and the power generator did not interfere with each other in the flow field.

(ii) The difference between the hydrodynamic coefficients before and after the power generator was equipped in the oblique sailing state was not large, and the relative error of the first-order linear hydrodynamic coefficient was within 7%. The hydrodynamic characteristics of the hull itself were not affected after the power generator was equipped. The distributions of the velocity field, pressure field, and vorticity field of the UUV with the power generator and the fully attached SUBOFF were similar at different drift angles, and only the area of the counter-rotating type turbine was different.

(iii) When the generator was working, the yaw moment N of the UUV was greater than the yaw moment when the generator was not equipped at most drift angles, but the overall trend of the two was similar. When the drift angle was 80°, the yaw moment of the UUV was 1.58 times that when the generator was not equipped, and the relative errors of the two were within 15% at other drift angles. The rotation of the counter-rotating type turbine did not damage the stability of the UUV hull in the moored state. In the process of changing the drift angle from 0° to 90°, the yaw moment of the UUV first increased and then decreased, and the critical point was approximately 50°.

(iv) When the UUV drift angle is small, it has a little impact on the performance of the turbine, but when the drift angle is greater than 50°, the existence of the UUV hull greatly affects the performance of the counter-rotating type turbine. The power coefficient C_P and thrust coefficient C_T increased by about 35.7% and 17.8%, respectively. When the UUV is mooring to generate electricity, the drift angle should be kept below 50° as much as possible.

Author Contributions: Conceptualization, S.W.; software, B.Z.; validation, J.S. and Y.Y.; formal analysis, J.S.; investigation, Y.Y.; resources, B.Z.; data curation, S.W.; writing—original draft preparation, J.S. and B.Z.; writing—review and editing, S.W., Y.Y. and B.H.; project administration, B.H.; funding acquisition, B.H. All authors have read and agreed to the published version of the manuscript.

Funding: This study was financially supported by National Natural Science Foundation of China (Grant No. 51839010 and 52076186; Funder ID: 10.13039/501100001809), the Key Research and Development Program of Zhejiang Province (Grant No. 2021C03133), and the Project of Bureau of Science and Technology of Zhoushan (No. 2022C81005).

Institutional Review Board Statement: Not applicable.

Informed Consent Statement: Not applicable.

Data Availability Statement: Not applicable.

Conflicts of Interest: The authors declare no conflict of interest.

References

1. Kuhlman, M.J.; Jones, D.; Sofge, D.A.; Hollinger, G.A.; Gupta, S.K. Collaborating underwater vehicles conducting large-scale geospatial tasks. *IEEE J. Ocean. Eng.* **2021**, *46*, 785–807. [CrossRef]
2. Li, D.; Du, L. Auv trajectory tracking models and control strategies: A review. *J. Mar. Sci. Eng.* **2021**, *9*, 1020. [CrossRef]
3. Glaviano, F.; Esposito, R.; Cosmo, A.D.; Esposito, F.; Gerevini, L.; Ria, A.; Molinara, M.; Bruschi, P.; Costantini, M.; Zupo, V. Management and Sustainable Exploitation of Marine Environments through Smart Monitoring and Automation. *J. Mar. Sci. Eng.* **2022**, *10*, 297. [CrossRef]
4. Capocci, R.; Dooly, G.; Omerdić, E.; Coleman, J.; Newe, T.; Toal, D. Inspection-class remotely operated vehicles—A review. *J. Mar. Sci. Eng.* **2017**, *5*, 13. [CrossRef]
5. Paull, L.; Saeedi, S.; Seto, M.; Li, H. AUV navigation and localization: A review. *Ieee J. Ocean. Eng* **2013**, *39*, 131–149. [CrossRef]
6. Salazar, T.; Youngblood, S.; Park, S. Underwater Environmental Impact and Thermal Management of Unmanned Underwater Vehicle Li-Ion Batteries. In Proceedings of the IECON 2021–47th Annual Conference of the IEEE Industrial Electronics Society, Toronto, Canada, 13–16 October 2021; IEEE: Piscataway, NJ, USA, 2021; pp. 1–5.
7. Toh, W.D.; Xu, B.; Jia, J.; Chin, C.S.; Chiew, J.; Gao, Z. Lithium iron phosphate ($LiFePO_4$) battery power system for deepwater emergency operation. *Energy Procedia* **2017**, *143*, 348–353. [CrossRef]
8. Mendez, A.; Leo, T.; Herreros, M. Current State of Technology of Fuel Cell Power Systems for Autonomous Underwater Vehicles. *Energies* **2014**, *7*, 4676–4693. [CrossRef]
9. Manley, J.E.; Smith, J. Rapid development and evolution of a micro-UUV. In *OCEANS 2017-Anchorage*; IEEE: Piscataway, NJ, USA, 2017; pp. 1–4.
10. Wilberforce, T.; El Hassan, Z.; Durrant, A.; Thompson, J.; Soudan, B.; Olabi, A.G. Overview of ocean power technology. *Energy* **2019**, *175*, 165–181. [CrossRef]
11. Sun, P.; Wu, X.; Cai, J.; Zhang, X.; Qiao, K.; Shen, H. Analysis of special technical problems of wireless charging at UUV docking stations and a new underwater electromagnetic coupler. *Energy Rep.* **2022**, *8*, 719–728. [CrossRef]
12. Sanborn, G.; Phipps, A. Standards and methods of power control for variable power bidirectional wireless power transfer. In Proceedings of the 2017 IEEE Wireless Power Transfer Conference (WPTC), Taipei, Taiwan, 10–12 May 2017; IEEE: Piscataway, NJ, USA, 2017; pp. 1–4.
13. Manalang, D.; Waters, B.; Smith, C.; LaMothe, P.; Carlson, M.; Yan, K. Adaptive Wireless Power for Subsea Vehicles. *Mar. Technol. Soc. J.* **2022**, *56*, 36–44. [CrossRef]
14. Santana Abril, J.; Santana Sosa, G.; Sosa, J.; Bautista, T.; Montiel-Nelson, J.A. A novel charging method for underwater batteryless sensor node networks. *Sensors* **2021**, *21*, 557. [CrossRef] [PubMed]
15. Cho, H.; Jeong, S.; Ji, D.; Tran, N.; Vu, M.T.; Choi, H. Study on control system of integrated unmanned surface vehicle and underwater vehicle. *Sensors* **2020**, *20*, 2633. [CrossRef]
16. Hu, H.; Xue, W.; Jiang, P.; Li, Y. Bibliometric analysis for ocean renewable energy: An comprehensive review for hotspots, frontiers, and emerging trends. *Renew. Sustain. Energy Rev.* **2022**, *167*, 112739. [CrossRef]
17. Uihlein, A.; Magagna, D. Wave and tidal current energy—A review of the current state of research beyond technology. *Renew. Sustain. Energy Rev.* **2016**, *58*, 1070–1081. [CrossRef]
18. Leng, J.; Wang, Q.; Li, Y. A geometrically nonlinear analysis method for offshore renewable energy systems—Examples of offshore wind and wave devices. *Ocean Eng.* **2022**, *250*, 110930. [CrossRef]
19. Buenau, K.E.; Garavelli, L.; Hemery, L.G.; García Medina, G. A Review of Modeling Approaches for Understanding and Monitoring the Environmental Effects of Marine Renewable Energy. *J. Mar. Sci. Eng.* **2022**, *10*, 94. [CrossRef]
20. Zhang, Y.; Yang, F.; Li, Y.; Qiu, W. Design and numerical investigation of a multi-directional energy-harvesting device for UUVs. *Energy* **2021**, *214*, 118978. [CrossRef]

21. Ding, W.; Song, B.; Mao, Z.; Zhao, X. Research on characteristics of power generation device for detection UUV by ocean kinetic energy in shallow water. *J. Xi'an Jiaotong Univ.* **2014**, *48*, 73–78.
22. Jung, H.; Subban, C.V.; McTigue, J.D.; Martinez, J.J.; Copping, A.E.; Osorio, J.; Liu, J.; Deng, Z.D. Extracting energy from ocean thermal and salinity gradients to power unmanned underwater vehicles: State of the art, current limitations, and future outlook. *Renew. Sustain. Energy Rev.* **2022**, *160*, 112283. [CrossRef]
23. Boye, H.; Caquot, E.; Clement, P.; de La Cochetiere, L.; Nataf, J.M.; Sergent, P. *Rapport de la Mission d'Étude sur les Énergies Marines Renouvelables*; Ministère de l'Écologie, du Développement Durable et de l'Énergie: Paris, France, 2013.
24. Khan, N.; Kalair, A.; Abas, N.; Haider, A. Review of ocean tidal, wave and thermal energy technologies. *Renew. Sustain. Energy Rev.* **2017**, *72*, 590–604. [CrossRef]
25. VanSwieten, J.H.; Meyer, I.; Alsenas, G.M. Evaluation of HYCOM as a tool for ocean current energy assessment. In Proceedings of the 2nd Marine Energy Technology Symposium, Seattle, WA, USA, 15–18 April 2014.
26. Hussain, A.; Arif, S.M.; Aslam, M. Emerging renewable and sustainable energy technologies: State of the art. *Renew. Sustain. Energy Rev.* **2017**, *71*, 12–28. [CrossRef]
27. Melikoglu, M. Current status and future of ocean energy sources: A global review. *Ocean Eng.* **2018**, *148*, 563–573. [CrossRef]
28. Li, L.; Zheng, J.; Peng, Y.; Zhang, J.; Wu, X. Numerical investigation of flow motion and performance of a horizontal axis tidal turbine subjected to a steady current. *China Ocean Eng.* **2015**, *29*, 209–222. [CrossRef]
29. Wang, S.; Chen, C.; Tan, J.; Yuan, P.; Zhou, X. Hydrodynamic performance of horizontal axis tidal current turbine based on blade element momentum theory. *Taiyangneng Xuebao/Acta Energiae Solaris Sin.* **2014**, *35*, 599–604.
30. Zhang, J.; Moreau, L.; Machmoum, M.; Guillerm, P. State of the art in tidal current energy extracting technologies. In Proceedings of the 2014 First International Conference on Green Energy ICGE, Sfax, Tunisia, 25–27 March 2014.
31. Tian, W.; Song, B.; Mao, Z. Numerical Analysis of a Water Turbine for Underwater Vehicles. *J. Shanghai Jiao Tong Univ.* **2013**, *47*, 1306–1311.
32. Wang, C.; Yang, F.; Nguyen, V.T.T.; Vo, N.T. CFD analysis and optimum design for a centrifugal pump using an effectively artificial intelligent algorithm. *Micromachines* **2022**, *13*, 1208. [CrossRef]
33. Chen, Z.; Nguyen, V.T.; Tran, N.T. Optimum design of the volute tongue shape of a low specific speed centrifugal pump. *J. Electr. Electron. Syst.* **2017**, *6*, 1–5. [CrossRef]
34. Zhao, T.; Gao, T.; Liu, P.; Zhang, B.; Liu, J. Design of energy harvesting system for low-power ocean current power generation. *Electron. Des. Eng.* **2020**, *28*, 70–75.
35. Samura, I.; Kuwano, K.; Kawashima, R.; Oda, T.; Imakyurei, T.; Inoue, H.; Tokunaga, Y.; Kanemoto, T.; Miyagawa, K.; Miwa, T. Counter-rotating type tidal stream power unit: Excellent performance verified at offshore test. In Proceedings of the IOP Conference Series: Earth and Environmental Science, Moscow, Russia, 27 May–6 June 2019; IOP Publishing: Bristol, UK, 2019; p. 52003.
36. Huang, B.; Kanemoto, T. Performance and internal flow of a counter-rotating type tidal stream turbine. *J. Therm. Sci.* **2015**, *24*, 410–416. [CrossRef]
37. Jung, H.; Kanemoto, T.; Liu, P.; Murakami, T. A numerical study on performance improvement of counter-rotating type tidal stream power unit. In Proceedings of the IOP Conference Series: Earth and Environmental Science, Moscow, Russia, 27 May–6 June 2019; IOP Publishing: Bristol, UK, 2019; p. 52013.
38. Lee, N.; Inagaki, M.; Kanemoto, T. Performance of counter-rotating tandem propellers at oblique flow conditions. In Proceedings of the IOP Conference Series: Earth and Environmental Science, Moscow, Russia, 27 May–6 June 2019; IOP Publishing: Bristol, UK, 2019; p. 52004.
39. Huang, B.; Zhu, G.J.; Kanemoto, T. Design and performance enhancement of a bi-directional counter-rotating type horizontal axis tidal turbine. *Ocean Eng.* **2016**, *128*, 116–123. [CrossRef]
40. Liu, X.; Hu, Y.; Mao, Z.; Tian, W. Numerical Simulation of the Hydrodynamic Performance and Self-Propulsion of a UUV near the Seabed. *Appl. Sci.* **2022**, *12*, 6975. [CrossRef]
41. Wang, P.; Zhao, B.; Cheng, H.; Huang, B.; He, W.; Zhang, Q.; Zhu, F. Study on the performance of a 300W counter-rotating type horizontal axis tidal turbine. *Ocean Eng.* **2022**, *255*, 111446. [CrossRef]
42. Karimi, M.; Akdogan, G.; Dellimore, K.H.; Bradshaw, S.M. Quantification of numerical uncertainty in computational fluid dynamics modelling of hydrocyclones. *Comput. Chem. Eng.* **2012**, *43*, 45–54. [CrossRef]
43. Stern, F.; Wilson, R.; Shao, J. Quantitative V&V of CFD simulations and certification of CFD codes. *Int. J. Numer. Methods Fluids* **2006**, *50*, 1335–1355.
44. Karaalioglu, M.S.; Bal, S. Performance prediction of cavitating marine current turbine by BEMT based on CFD. *Ocean Eng.* **2022**, *255*, 111221. [CrossRef]
45. Craft, T.J.; Gant, S.E.; Gerasimov, A.V.; Iacovides, H.; Launder, B.E. Wall-function strategies for use in turbulent flow CFD. In Proceedings of the International Heat Transfer Conference Digital Library, Grenoble, France, 18–23 August 2002; Begel House Inc.: Danbury, CT, USA, 2002.
46. Huang, B.; Zhao, B.; Wang, L.; Wang, P.; Zhao, H.; Guo, P.; Yang, S.; Wu, D. The effects of heave motion on the performance of a floating counter-rotating type tidal turbine under wave-current interaction. *Energy Convers. Manag.* **2022**, *252*, 115093. [CrossRef]